

FUSION OF PHYSICS-BASED MODELS WITH FIELD MEASUREMENTS FOR TURBULENT FLOW RECONSTRUCTION

C Vamsi Krishna

Aerospace and Mechanical Engineering
University of Southern California
Los Angeles, CA 90089
vchinta@usc.edu

Mengying Wang

Aerospace Engineering and Mechanics
University of Minnesota,
Minneapolis, MN 55455
wang5772@umn.edu

Maziar Hemati

Aerospace Engineering and Mechanics
University of Minnesota
Minneapolis, MN 55455
mhemati@umn.edu

Mitul Luhar

Aerospace and Mechanical Engineering
University of Southern California
Los Angeles, CA 90089
mluhar@usc.edu

ABSTRACT

Particle Image Velocimetry (PIV) systems are often limited in their ability to fully resolve the broadband temporal fluctuations associated with turbulent flows due to hardware limitations or cost constraints. In this study, we use physics-based models grounded in Rapid Distortion Theory (RDT) to reconstruct the time evolution of wall-bounded turbulent flows between consecutive PIV snapshots. The linear RDT equations are integrated forwards and backwards in time from the PIV snapshots, and the flow field in the intervening period is estimated via a weighted summation of these forward- and backward-time estimates. The weights used for this fusion are formulated to account for the advective nature of the RDT equations. The backward-time integration is unstable over longer time horizons due to negative diffusion. To overcome this problem, the linear RDT equations are further simplified to retain just the advective term. In other words, Taylor's frozen turbulence hypothesis is employed for the backward-time integration. Reconstruction accuracy is evaluated as a function of spatial resolution and time horizon using Direct Numerical Simulation (DNS) data for turbulent channel flow from the Johns Hopkins Turbulence Database.

INTRODUCTION

Laboratory instruments are often limited in their ability to fully resolve the broadband spatiotemporal fluctuations associated with turbulent flows. Field measurement techniques, such as Particle Image Velocimetry (PIV), can have high spatial resolution but are typically restricted in temporal resolution due to hardware limitations or cost constraints. Conversely, techniques such as Hot-Wire Anemometry (HWA) that have high temporal resolution are limited to point measurements.

To bridge this gap in diagnostic capabilities, a number of previous studies have fused time-resolved point data with spatially-resolved field data for flow reconstruction. Most of these efforts reconstruct the flow via projection onto spatial basis functions obtained from field data (e.g.,

modes from proper orthogonal or dynamic mode decomposition). Time-resolved data are then used to infer the temporal variation of mode amplitude (Tu *et al.*, 2013; Berry *et al.*, 2017; Discetti *et al.*, 2018). However, this approach requires extensive prior data and there is no guarantee that the reconstructed flow field will be physically sound, i.e., satisfy the governing equations. Recent efforts have also employed basis functions obtained directly from the governing Navier-Stokes equations (NSE) for reconstruction. For example, Gómez *et al.* (2016) projected velocity measurements from a bluff body wake onto resolvent modes to estimate the unsteady aerodynamic forces. Similarly, Beneddine *et al.* (2017) employed a resolvent-based framework to reconstruct the full flow field for a round jet based on a single point measurement.

Building on these previous efforts, which have primarily considered narrow-banded flows (e.g., wakes, jets), the present study seeks to create a physics-based framework for reconstruction of more complex wall-bounded turbulent flows. Specifically, we employ models grounded in Rapid Distortion Theory (RDT), which has strong connections with resolvent analysis (McKeon, 2017), to reconstruct the time-evolution of such flows from 'slow' field measurements (e.g., from non time-resolved PIV). To test this reconstruction framework, we employ direct numerical simulation (DNS) data for turbulent channel flow at friction Reynolds number $Re_\tau = 1000$ from the Johns Hopkins Turbulence Database (JHTDB, see e.g., Graham *et al.*, 2016). This is a step towards the development of a mathematical framework that can be used to fuse such 'slow' field measurements with 'fast' point measurements (e.g., from HWA) to reconstruct the flow field in a physically consistent manner via Bayesian optimal estimation.

METHODS Theory

To reconstruct the velocity field between two consecutive PIV snapshots in a turbulent channel flow, we use models grounded in RDT, which linearizes the NSE about

a mean profile (Batchelor & Proudman, 1954; Savill, 1987; Hunt & Carruthers, 1990) to yield the following momentum equation and continuity constraint:

$$\frac{\partial \mathbf{u}}{\partial t} + \mathbf{U} \cdot \nabla \mathbf{u} + \mathbf{u} \cdot \nabla \mathbf{U} = -\nabla p + \frac{1}{Re_\tau} \nabla^2 \mathbf{u} + (NL), \quad (1)$$

and

$$\nabla \cdot \mathbf{u} = 0. \quad (2)$$

In the expressions above, $\mathbf{U} = (U(y), 0, 0)$ represents the mean profile, $\mathbf{u} = (u, v, w)$ denotes the turbulent velocity fluctuations, p is pressure, and (NL) represents the (neglected) nonlinear terms. A standard Cartesian coordinate system is used, in which x is the streamwise direction, y is the wall-normal direction, and z is the spanwise direction; t is time.

Scaling arguments show that the nonlinear terms can be neglected in turbulent shear flows for time horizons that are shorter than the typical eddy turnover time (Savill, 1987; Hunt & Carruthers, 1990). This makes RDT an appropriate choice for the present problem requiring temporal reconstruction between sequential PIV snapshots. However, even with the substantial simplification afforded by linearization, reconstruction based on the full RDT equations is likely to be difficult in practice. This is because most common PIV systems are only capable of generating two-dimensional/two-component (2D-2C) field measurements. Assuming these PIV measurements are carried out in the (x, y) plane to yield velocity components (u, v) , additional simplifying assumptions are needed to account for the out-of-plane flow and pressure gradient terms. Here, we simply neglect these terms to yield the following coupled advection-diffusion equations:

$$\underbrace{\frac{\partial u}{\partial t} + U \frac{\partial u}{\partial x}}_{\text{advection term}} = \underbrace{\frac{1}{Re_\tau} \left(\frac{\partial^2 u}{\partial x^2} + \frac{\partial^2 u}{\partial y^2} \right)}_{\text{diffusion term}} - \underbrace{v \frac{\partial U}{\partial y}}_{\text{coupling term}} \quad (3)$$

and

$$\underbrace{\frac{\partial v}{\partial t} + U \frac{\partial v}{\partial x}}_{\text{advection term}} = \underbrace{\frac{1}{Re_\tau} \left(\frac{\partial^2 v}{\partial x^2} + \frac{\partial^2 v}{\partial y^2} \right)}_{\text{diffusion term}} \quad (4)$$

The equations above can be further simplified by assuming that the advection term is dominant – equivalent to Taylor’s frozen turbulence hypothesis – which yields

$$\frac{\partial \mathbf{u}}{\partial t} + U \frac{\partial \mathbf{u}}{\partial x} = 0. \quad (5)$$

Below, we employ the linear models in (3)-(5) to reconstruct the evolution of a turbulent channel flow between two 2D-2C field measurement snapshots (e.g., from PIV) separated by time interval T .

Note that reconstruction can proceed both forwards and backwards in time. In other words, the equations above can be integrated forwards in time using the first snapshot

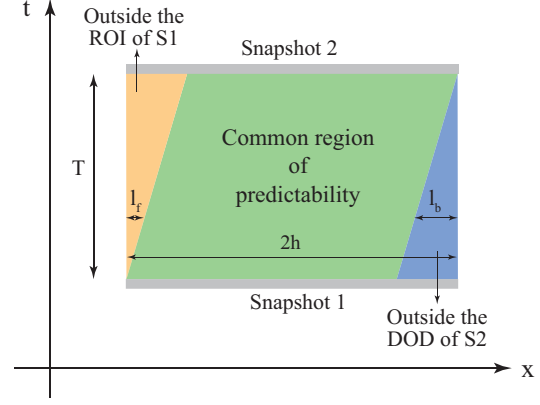


Figure 1. Schematic $x-t$ diagram for the snapshots at a given y location. The interfaces between the different colors correspond to characteristic lines originating from each snapshot. These characteristics depend on the local mean velocity, $U(y)$. The yellow region on the left-hand side of this diagram is outside the region of influence (ROI) for snapshot 1 (S1). Here, only the backward-time estimate is used. Similarly, the blue region on the right-hand side is outside the domain of dependence (DOD) for snapshot 2 (S2). Here, only the forward-time estimate is used. The green region lies within the ROI and DOD of both snapshots. Here, the reconstructed velocity field is a weighted sum of both the forward and backward predictions.

as the initial condition, as well as backwards in time using the second snapshot as the initial condition. Moreover, an appropriately weighted combination of these forward- and backward-time estimates has the potential to improve reconstruction accuracy. Below, we develop physically-motivated weighting schemes for this fusion.

Fusion of Forward and Backward Estimates

A simple way to fuse the forward ($\hat{\mathbf{u}}_f$) and backward ($\hat{\mathbf{u}}_b$) estimates is to use weights that vary linearly in time

$$k_f = 1 - \frac{t}{T}; \quad k_b = \frac{t}{T}. \quad (6)$$

Here $t = 0$ corresponds to the initial snapshot and $t = T$ corresponds to the final snapshot, and the reconstructed flow field is given by

$$\hat{\mathbf{u}}_{fb} = k_f \hat{\mathbf{u}}_f + k_b \hat{\mathbf{u}}_b. \quad (7)$$

This particular weighting scheme ensures that the forward-time estimate is weighted more heavily closer to the initial snapshot and the backward-time estimate is weighted more heavily towards the final snapshot.

This weighting scheme can be improved further by considering the mathematical nature of the equations emerging from RDT and Taylor’s hypothesis (TH). Assuming that the hyperbolic advection term is dominant, information is expected to propagate at a speed corresponding to the local mean velocity. This is illustrated in the $x-t$ diagram shown in figure 1. The region of influence (ROI) for

the first snapshot and the domain of dependence (DOD) for the second snapshot are determined by characteristics in the $x-t$ plane that have slope $dt/dx = 1/U(y)$. The forward-time estimate is expected to be accurate only in the ROI of the first snapshot (i.e., green and blue regions in figure 1) while the backward-time estimate is expected to be accurate only in the DOD of the second snapshot (i.e., yellow and green regions in figure 1). Further, since the slope of the characteristics varies in the y direction, the size of the ROI and DOD also vary with y .

To account for these effects, the weighting scheme in (6) can be modified as follows. The linear weighting scheme in (6) can be retained in the common region of predictability for both snapshots (green region in figure 1). The forward weight, k_f , is set to 0 in the region outside the ROI of the first snapshot (yellow region in figure 1) and the backward weight, k_b , is set to 1. Similarly, $k_f = 1$ in the region outside the DOD of the second snapshot (blue region in figure 1) and $k_b = 0$. The resulting equations for weights are:

$$k_f(x, y, t) = \begin{cases} 0 & 0 \leq x < l_f \\ (1 - \frac{t}{T}) & l_f \leq x \leq 2h - l_b \\ 1 & 2h - l_b < x \leq 2h, \end{cases} \quad (8)$$

and

$$k_b(x, y, t) = \begin{cases} 1 & 0 \leq x < l_f \\ \frac{t}{T} & l_f \leq x \leq 2h - l_b \\ 0 & 2h - l_b < x \leq 2h. \end{cases} \quad (9)$$

where $l_f = U(y)t$ and $l_b = U(y)(T - t)$. Note that the weights are now dependent on (x, y) as well as t .

Numerical Evaluation

To test reconstruction accuracy for the forward, backward, and fused estimates, we use DNS data for turbulent channel flow at $Re_\tau = 1000$ available from the JHTDB (Graham *et al.*, 2016). For consistency with typical PIV systems, we only use 2D-2C velocity data in the $x-y$ plane that is sampled uniformly in time and space. The full dataset acquired includes 512 snapshots obtained at intervals of $\delta t^+ = 0.0625$, where a superscript $+$ denotes normalization with respect to the friction velocity u_τ and viscosity ν . Thus, the total time interval between the first and last snapshots is $T^+ = 512 \times \delta t^+ = 32$. The field of view is of size $2h^+ \times 2h^+$, where $h^+ = Re_\tau$ is the inner-normalized channel half-height. The grid resolution is $\Delta x^+ = \Delta y^+ \approx 4$.

Equations (3)-(5) are numerically integrated forwards and backwards in time from the first and last snapshots, respectively. A standard finite difference scheme is used for this purpose. An explicit Euler method is used for time integration, a first-order upwinding scheme is used for the advection term, and a second-order central differencing scheme is used for the diffusion and coupling terms.

Only the first and last DNS snapshots are used to reconstruct the flow field. The intervening snapshots are used to quantify reconstruction accuracy using the error metrics

$$\varepsilon(t) = \frac{\int_{x=0}^{2h} \int_{y=0}^{2h} \left((u - \hat{u})^2 + (v - \hat{v})^2 \right) dx dy}{\int_{x=0}^{2h} \int_{y=0}^{2h} (\hat{u}^2 + \hat{v}^2) dx dy} \quad (10)$$

and

$$\varepsilon(y, t) = \frac{\int_{x=0}^{2h} \left((u - \hat{u})^2 + (v - \hat{v})^2 \right) dx}{\int_{x=0}^{2h} (\hat{u}^2 + \hat{v}^2) dx} \quad (11)$$

where u and v are the reconstructed velocity fluctuations, and \hat{u} and \hat{v} are the velocity fluctuations from DNS ‘truth’. Reconstruction accuracy is evaluated for the forward and backward estimates individually, as well as for the fused estimates. We also provide a brief evaluation of the effect of field measurement spatial resolution ($\Delta x^+ = \Delta y^+$) and time horizon (T^+) on reconstruction accuracy.

RESULTS AND DISCUSSION

As a baseline test, we first evaluate reconstruction error using the different methods discussed above over a time horizon $T^+ \approx 16$. For reference, the error associated with a direct linear interpolation between the two images is plotted as a black line in figure 2. As expected, linear interpolation yields lower error closest to the snapshots (i.e., at the beginning and end of the time horizon). The maximum reconstruction error associated with linear interpolation is $\varepsilon \approx 0.8$. The forward-time RDT prediction (blue line) performs much better initially than the linear interpolation. However, the error associated with this technique increases monotonically with time and exceeds the error associated with linear interpolation after $t^+ \approx 10$. This is because linear interpolation relies on information from both the initial and final snapshots, while the forward-time RDT model only uses information from the initial snapshot. To overcome this limitation, we can also include information from the backward-time RDT predictions, which have significantly lower error towards the end of the prediction time horizon (red line). The reconstruction that fuses the forward- and backward-time RDT estimates based purely on the temporal weights shown in (6) leads to a maximum error of $\varepsilon \approx 0.5$ (turquoise line), which is significantly lower than the maximum error from linear interpolation. The spatiotemporal weighting scheme shown in (8)-(9) reduces the maximum error even further to $\varepsilon \approx 0.3$ (green line).

The wall-normal distribution of the reconstruction error for the best performing technique (i.e., forward- and backward-time RDT models fused with the spatiotemporal weighting scheme) is shown in figure 2(b). The error is higher in the inner region of the flow, below $y/h \approx 0.2$ or $y^+ \approx 200$, where turbulent kinetic energy — and turbulence production — are higher. Further, the error appears to peak in the logarithmic region of the flow, near $y^+ \approx 50$. However, this observation must be treated with some caution. Due to the linear distribution of grid points in the wall-normal direction, there is insufficient spatial resolution to provide a detailed evaluation of the reconstruction error in the buffer layer. As expected, for a given wall-normal location, the reconstruction error follows a similar trend as in figure 2(a). The reconstruction error is maximum in the middle of the time horizon and goes to 0 at the beginning and the end.

Figure 3 compares DNS results for the time-varying streamwise and wall-normal velocity fluctuations (a,b) in the center of the streamwise domain being considered here with the corresponding fused RDT reconstructions (c,d). Similarly, figure 4 compares a snapshot of the fluctuating

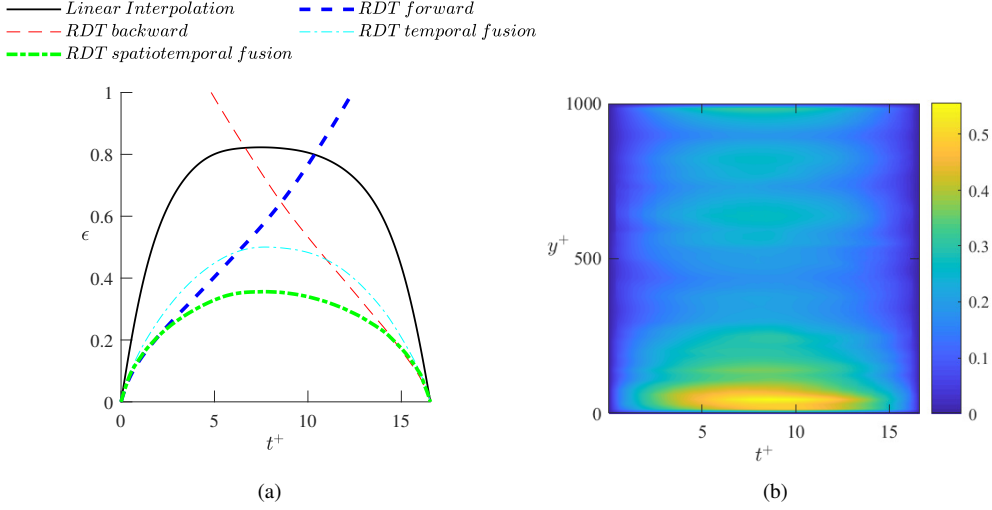


Figure 2. (a) Evolution of reconstruction error with time, computed using (10), for different methods: direct linear interpolation (black), forward-time RDT (blue line), backward-time RDT (red line), fused RDT with temporal weights (turquoise line), and fused RDT with spatiotemporal weights (green line). (b) Reconstruction error as a function of time and the wall-normal coordinate, computed using (11), for the fused RDT estimate with spatiotemporal weighting. The contour plot is shown from the wall ($y^+ = 0$) to the channel centerline ($y^+ = 1000$).

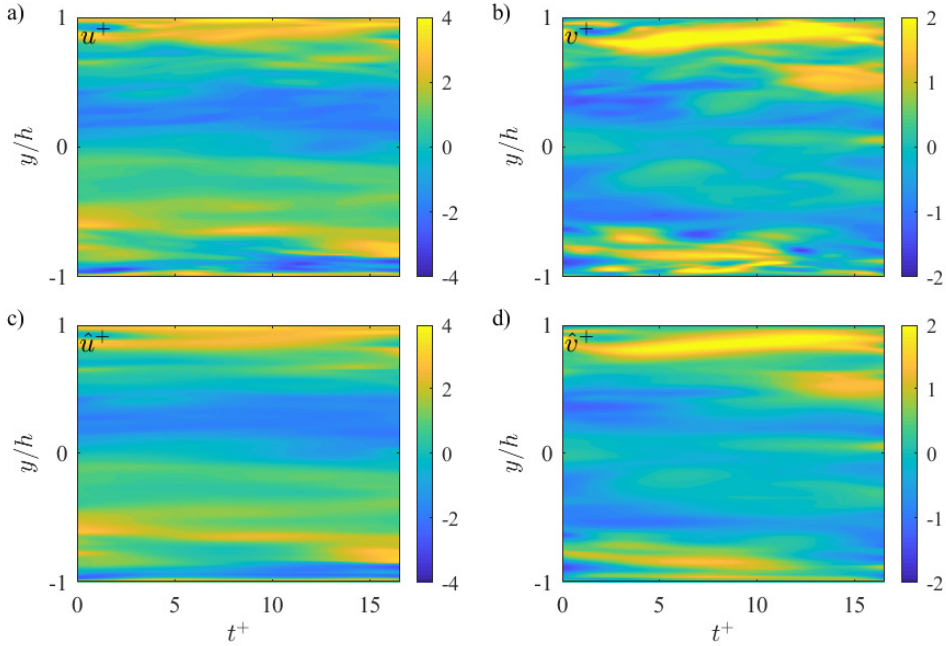


Figure 3. Comparison between the temporal evolution of the reconstructed velocity fluctuations and DNS results. Subfigures (a) and (b) show DNS results for the horizontal and vertical velocity fluctuations as a function of time in the middle of the streamwise domain considered here. Reconstructed velocity fluctuations at the same streamwise location are shown in subfigures (c) and (d). These predictions correspond to the fused RDT model with the spatiotemporal weighting scheme.

velocity field from DNS (a,b) at the middle of the time horizon, where the reconstruction error is expected to be highest, with the fused RDT estimate (c,d). These figures confirm that the RDT-based reconstruction qualitatively reproduces both the time-variation and spatial distribution of the fluctuating velocities. Although the spatiotemporal weighting scheme in (8) and (9) has spatial ‘shocks’, this is not reflected in the reconstructed snapshot. A further evaluation (not shown here) does show the presence of discontinuous velocity gradients in the reconstructed snapshot. In general,

the reconstructed flow fields do appear smoother than the DNS results. This smoothing process could be attributed to the fact that the nonlinear terms and the out-of-plane component of the flow are neglected, which limits energy transfer to small-scales. The lower spatial resolution used for reconstruction compared to the DNS could also play a role. Future work will evaluate whether reconstruction based on 3D snapshots (e.g., from tomographic PIV) and RDT yield reduced errors.

The effect of grid size ($\Delta x^+ = \Delta y^+$) and prediction time

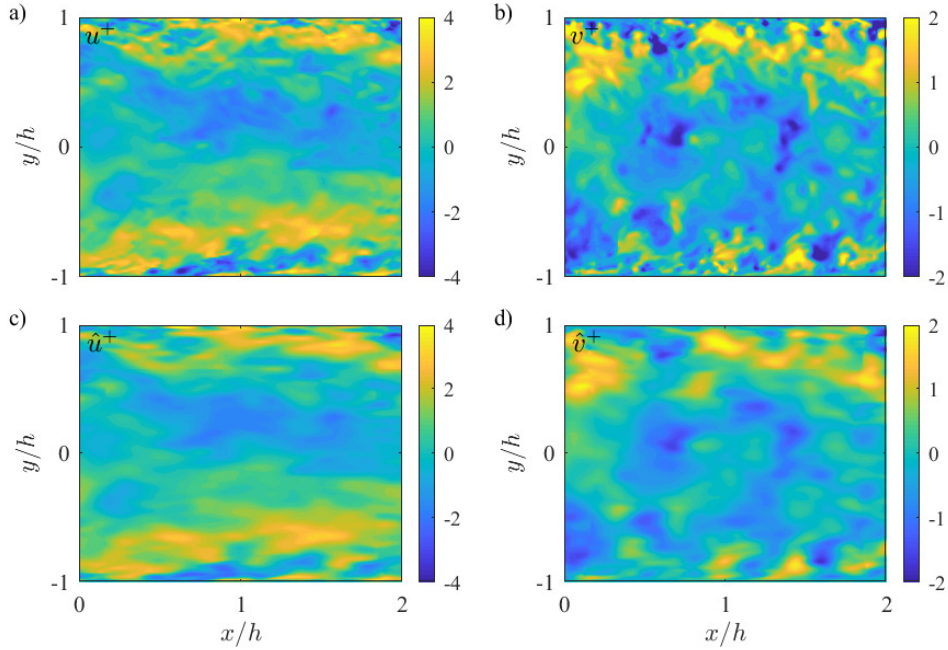


Figure 4. Comparison between the reconstructed velocity field and DNS results. Subfigures (a) and (b) show snapshots of the horizontal and vertical velocity fluctuations obtained in DNS in the middle of the time horizon being considered, i.e. at $t^+ \approx 8$, where the reconstruction error is maximum. Reconstructed velocity fluctuations at the same time instant are shown in subfigures (c) and (d). Once again, these predictions correspond to the fused RDT model with the spatiotemporal weighting scheme.

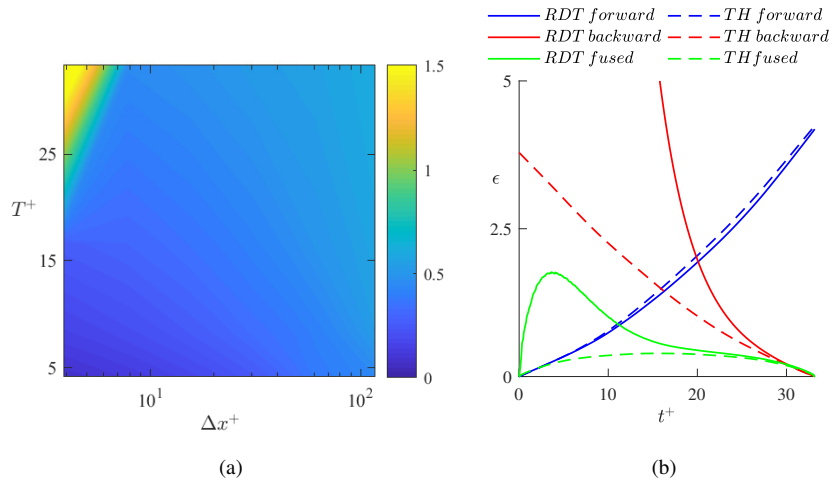


Figure 5. (a) Maximum reconstruction error using the fused RDT model as a function of grid resolution and prediction time horizon. The top left corner of the plot shows that as T^+ increases, the prediction error increases dramatically for fine spatial resolutions. (b) Reconstruction error using the RDT models (solid lines) and Taylor's hypothesis (dashed lines) for $\Delta x^+ = 4$ and $T^+ = 32$ for the forward-time integration (blue line), backward time integration (red lines) and the fused estimate (green lines). Error for the backward-time RDT model increases rapidly towards the beginning of the prediction window. Error for backward-time Taylor's hypothesis estimate increases at a much slower rate. This leads to a substantial decrease in error for the fused Taylor's hypothesis estimate (dashed green line).

horizon (T^+) on maximum reconstruction error with the fused RDT model is shown in figure 5(a). In general, the reconstruction error decreases with decreasing Δx^+ and T^+ . However, for $T^+ \geq 24$, the error increases dramatically with a decrease in grid size (top left corner of figure 5(a)). This is because the viscous diffusion term is unstable when integrating backwards in time, i.e., backward time integration

effectively yields a negative viscosity, which enhances velocity gradients. As shown in figure 5(b), this effect dominates the backward-time RDT estimates (solid red line) over long time horizons.

To overcome this problem, we use Taylor's hypothesis (TH) for reconstruction, which assumes that the flow is dominated by the advection term. The diffusion and cou-

pling terms are neglected leading to (5). With just the advection term, the governing equations are hyperbolic in nature and the spatiotemporal weighting scheme shown in (8)-(9) is appropriate for fusion of the forward- and backward-time reconstructions. As shown in figure 5(b), the accuracy of reconstruction with Taylor's hypothesis is similar to that with RDT for the forward-time reconstruction. The forward-time RDT estimate only yields a minor reduction in reconstruction error. However, for the backward-time estimate, Taylor's hypothesis outperforms RDT significantly. Hence, the error for the fused reconstruction under Taylor's hypothesis is also much lower than that for the fused RDT model.

CONCLUSION

The results presented in this paper show that both RDT and Taylor's hypothesis provide useful models for the reconstruction of turbulent flows from 'slow' field measurements. The forward-time reconstruction accuracy is comparable for both classes of models. However, the backward-time RDT dynamics are unstable, degrading reconstruction over longer time horizons. Overall, this makes models grounded in Taylor's hypothesis more attractive when reconstruction is required over longer time horizons. This also motivates the need for more formal dynamic estimation that can stabilize the error dynamics.

The success of Taylor's hypothesis and the spatiotemporal weighting illustrated schematically in figure 1 is not surprising given the advection-dominated nature of wall-bounded turbulent shear flows. Indeed, Taylor's hypothesis has been used extensively to translate time-resolved velocity measurements (e.g., from HWA) into spatial flow fields and wavenumber spectra in prior turbulence literature (e.g., Wyngaard & Clifford, 1977; Dennis & Nickels, 2008; Moin, 2009). Here, we use Taylor's hypothesis to translate spatially-resolved field measurements into improved temporal resolution. Note that improved temporal resolution is only possible if the measurement spatial resolution is high enough to ensure that the frequency corresponding to the spatial Nyquist limit $f_s^+ = U^+/(2\Delta x^+)$ is higher than the temporal Nyquist frequency $f_t^+ = 1/(2T^+)$. Moreover, the spatiotemporal weighting scheme shown in figure 1 can only be used in cases where $U^+T^+ \leq L_x^+$, where L_x^+ is the streamwise length of the measurement domain. If this condition is not satisfied, portions of the $x-t$ plane may fall outside of the ROI of snapshot 1 and outside the DOD of snapshot 2.

Moving forward, this research effort will verify the spatiotemporal limits discussed in the previous paragraph quantitatively. Reconstruction from 3D snapshots will also be attempted to inform the development of 2D models that improve upon the simple — and admittedly ad-hoc — relations shown in (3)-(5). Ultimately, this work will feed into the development of a dynamic estimation framework that can fuse information from multiple noisy and uncertain field or point measurements and physics-based models in a statistically optimal manner.

ACKNOWLEDGMENTS

CVK is grateful for financial support from the graduate school at University of Southern California through the Provost fellowship.

REFERENCES

- Batchelor, GK & Proudman, Ian 1954 The effect of rapid distortion of a fluid in turbulent motion. *The Quarterly Journal of Mechanics and Applied Mathematics* **7** (1), 83–103.
- Beneddine, Samir, Yegavian, Robin, Sipp, Denis & Leclaire, Benjamin 2017 Unsteady flow dynamics reconstruction from mean flow and point sensors: an experimental study. *Journal of Fluid Mechanics* **824**, 174–201.
- Berry, Matthew G, Stack, Cory M, Magstadt, Andrew S, Ali, Mohd Y, Gaitonde, Datta V & Glauser, Mark N 2017 Low-dimensional and data fusion techniques applied to a supersonic multistream single expansion ramp nozzle. *Physical Review Fluids* **2** (10), 100504.
- Dennis, David JC & Nickels, Timothy B 2008 On the limitations of Taylor's hypothesis in constructing long structures in a turbulent boundary layer. *Journal of Fluid Mechanics* **614**, 197–206.
- Discetti, Stefano, Raiola, Marco & Ianiro, Andrea 2018 Estimation of time-resolved turbulent fields through correlation of non-time-resolved field measurements and time-resolved point measurements. *Experimental Thermal and Fluid Science* **93**, 119–130.
- Gómez, F, Sharma, AS & Blackburn, HM 2016 Estimation of unsteady aerodynamic forces using pointwise velocity data. *Journal of Fluid Mechanics* **804**.
- Graham, J, Kanov, K, Yang, XIA, Lee, M, Malaya, N, Lalescu, CC, Burns, R, Eyink, G, Szalay, A, Moser, RD *et al.* 2016 A web services accessible database of turbulent channel flow and its use for testing a new integral wall model for LES. *Journal of Turbulence* **17** (2), 181–215.
- Hunt, Julian CR & Carruthers, David J 1990 Rapid distortion theory and the 'problems' of turbulence. *Journal of Fluid Mechanics* **212**, 497–532.
- McKeon, BJ 2017 The engine behind (wall) turbulence: perspectives on scale interactions. *Journal of Fluid Mechanics* **817**.
- Moin, P 2009 Revisiting Taylor's hypothesis. *Journal of Fluid Mechanics* **640**, 1–4.
- Savill, AM 1987 Recent developments in rapid-distortion theory. *Annual Review of Fluid Mechanics* **19** (1), 531–573.
- Tu, Jonathan H, Griffin, John, Hart, Adam, Rowley, Clarence W, Cattafesta, Louis N & Ukeiley, Lawrence S 2013 Integration of non-time-resolved piv and time-resolved velocity point sensors for dynamic estimation of velocity fields. *Experiments in fluids* **54** (2), 1429.
- Wyngaard, JC & Clifford, SF 1977 Taylor's hypothesis and high-frequency turbulence spectra. *Journal of the Atmospheric Sciences* **34** (6), 922–929.